PAPER

Check for updates

Preparation and photocatalytic degradation of methylene blue using a sulfanilic acid-functionalized NiO/GO ternary composite with electrochemical evaluation

Huma Sadiq, [ID] *[a] Hanan Sadiq, [ID] [a] Alejandra Garcia-Garcia,[a] Luz Idalia Ibarra Rodriguez,[a] Kiran Batool,[b] Hafiza Hira Sharif[c] and Maha Sharif*[d]

A NiO/GO/SA ternary nanocomposite was successfully synthesized *via* co-precipitation and demonstrated multifunctional performance. Structural analysis confirmed uniform NiO distribution on wrinkled GO sheets with sulfanilic acid functionalization, yielding reduced crystallite size (~18–22 nm), high crystallinity (83%), and strong interfacial bonding, as verified by Raman, FTIR, and XPS. Elemental mapping further validated the integration of Ni, O, C, S, and N functionalities, which contribute to the composite's synergistic properties. The photocatalyst exhibited excellent visible-light activity against methylene blue, achieving 96% degradation with pseudo-first-order kinetics ($k = 0.032$ min^{-1}) and 82% TOC mineralization after 210 min. Radical scavenger studies confirmed hydroxyl and superoxide radicals as the dominant species. The composite outperformed several reported ternary systems and retained >85% efficiency after five reuse cycles, demonstrating both activity and stability. Electrochemical studies showed pseudocapacitive behavior with reversible Ni^{2+}/Ni^{3+} redox transitions, low charge-transfer resistance (~0.4 kΩ), and high capacitance of 650 F g^{-1} at 5 mV s^{-1}, maintaining 275 F g^{-1} at 50 mV s^{-1}. These results highlight NiO/GO/SA as a promising material for wastewater treatment and energy storage, with potential improvements achievable through further interface engineering and defect modulation.

1 Introduction

The discharge of synthetic dyes into water bodies from industrial activities such as textile manufacture,[1] leather processing,[2] plastics production,[3] and paper bleaching poses a major environmental challenge.[4] These dyes, often non-biodegradable and chemically stable, persist in aquatic systems, causing aesthetic pollution, reducing light penetration, and adversely affecting aquatic life.[5] Among the widely used dyes, methylene blue is a cationic thiazine dye commonly employed in various applications.[6] Despite its industrial utility, MB exhibits notable cytotoxic effects, including eye irritation, respiratory complications, and potential mutagenicity, thereby necessitating its efficient removal from wastewater.[7]

Traditional treatment methods such as adsorption, coagulation, and biological degradation frequently fail to achieve complete removal of such dyes due to their resistance to degradation and complex aromatic structures.[8] As a result, advanced oxidation processes (AOPs), particularly semiconductor-assisted photocatalysis, have emerged as effective techniques for degrading recalcitrant organic pollutants. Photocatalysis utilizes light-activated semiconductors to generate electron–hole pairs, which subsequently produce reactive oxygen species (ROS) capable of breaking down dye molecules into harmless by-products.[9] The photocatalyst's influenced very strong by its light absorption and charge carrier separation and transport efficiencies.[10]

Nickel oxide (NiO), a p-type semiconductor, investigated for its photocatalytic properties owing to its thermal and chemical stability, non-toxicity, and earth abundance.[11] However, the practical use of NiO is constrained by its wider bandgap (approximately 3.6–4.0 eV),[12] which limits light absorption to the Ultraviolet domain, and by the higher photogenerated carriers recombination.[13]

To address these limitations, graphene oxide (GO) is frequently incorporated into photocatalytic systems. GO's high specific surface area and rich functional group chemistry enhance its ability to act as a conductive scaffold,[14] improving charge carrier separation and reducing recombination.[15] Additionally, the two-dimensional structure of GO provides a favorable platform for dye adsorption and light harvesting, further boosting photocatalytic activity.[16]

[a]Department of Material Science, CIMAV Unidad Monterrey, Apodaca, Nuevo Leon, Mexico. E-mail: huma.sadiq@cimav.edu.mx

[b]College of Materials Science and Engineering, Shenzhen University, Shenzhen 518060, China

[c]Department of Physics, Virtual University of Pakistan, Pakistan

[d]Department of Chemistry, Wake Forest University, USA. E-mail: sharm22@wfu.edu

The functionalization of such composites with sulfanilic acid (SA) introduces additional benefits. The direct band gap of sulfanilic acid is 4.23 eV.[17] SA contains both sulfonic and amine groups, which enhance the hydrophilicity and dispersibility of the nanomaterials in aqueous media.[18] These groups also contribute to improved surface charge characteristics and may facilitate visible light absorption.[19] Moreover, the aromatic nature of SA can promote π–π interactions with dye molecules, aiding in enhanced adsorption of MB and subsequent degradation.[20] Although NiO (3.7 eV) and SA (4.23 eV) are wide-bandgap materials, their combination with GO facilitates visible-light photocatalytic activity. GO acts as an electron acceptor and conductive scaffold, enhancing charge separation, reducing recombination, and providing additional adsorption sites, enabling efficient degradation of methylene blue under visible light.

This work presents the synthesis of a ternary NiO/GO/SA nanocomposite through a simple and scalable method to enhance photocatalytic performance under visible light. Unlike previously reported NiO/GO-based ternary systems, the incorporation of sulfanilic acid introduces both amine and sulfonic functional groups, which simultaneously improve interfacial charge transport, hydrophilicity, and π–π interaction with aromatic dye molecules. The ternary composite was systematically characterized and evaluated for methylene blue degradation under visible light. The observed synergistic composite exhibits effects from GO and SA enhancing charge separation, increased surface adsorption, and greater light utilization demonstrate that NiO/GO/SA is not merely more efficient but also distinct from other NiO-based ternary photocatalysts. These findings highlight its potential as a low-cost and environmentally friendly photocatalyst for dye-polluted wastewater remediation.

2 Experimental procedure

2.1 Material required

Nickel oxide, graphene oxide, sulfanilic acid, distilled water, NaOH, KMnO$_4$, H$_2$O$_2$ were supplied by Sigma Aldrich and without any purification.

2.2 Synthesis of graphene oxide

Graphene oxide (GO) prepared using a modified Hummer's method.[21] 1 g of graphite powder was sonicated in a sonicator for 40 min with a 3 : 1 volumetric ratio of H$_2$SO$_4$ and nitric acid. 9 grams of KMnO$_4$ were added slowly while maintaining a temperature of 5 °C. 200 mL of deionized water was added in drops while continuing to stir for one hour. The solution was then stirred for one day, followed by the addition of 30 mL of hydrogen peroxide to stop the reaction. After the addition of H$_2$O$_2$, the color of the solution changed, confirming the presence of graphene oxide.

2.3 Synthesis of ternary nanocomposite

A ternary nanocomposite of NiO/GO/SA was synthesized by using the co-precipitation method, as shown in Fig. 1. 2 mL of as prepared GO suspension ($\sim$4 mg mL^{-1}) was mixed with 50 mL of distilled water and then sonicated for 15 minutes. In another vessel, 0.1 M solution of nickel salt and sulfanilic acid are mixed in 25 mL of deionized (DI) water and then combined with graphene oxide after 15 minutes. Prepare a 0.1 M solution of NaOH in 25 mL of deionized (DI) water and add it dropwise while maintaining the temperature. Keep stirring the final solution for 1 hour on a hot plate at 70 °C. Centrifuge the final solution at 4000 rpm for 20 minutes, and the precipitate obtained was then baked in an oven for 3 hours at 70 °C.

2.4 Methylene blue photocatalytic degradation under visible light

The degradation of methylene blue was used to determine the photocatalytic activity of NiO/SA/GO. 200 mL of distilled water was placed in a test tube, and then 0.02 g of methylene blue (100 ppm) was added to it. The visible light source with intensity 80 (W m^{-2}) was used for photodegradation. First, 4 mL of MB sample was taken. Then, the catalyst was added and stirred for 1 hour in dark light. After adding the catalyst, the reaction mixture was exposed to visible-light irradiation, and the timer was started. Then sample were withdrawn every 30 minutes for a total duration of 3 hours to monitor the photocatalytic degradation of methylene blue.

2.5 Total organic carbon (TOC) measurement procedure

The mineralization of methylene blue (MB) during photocatalytic degradation was evaluated using total organic carbon (TOC) analysis. Experiments were conducted using 0.001 g of MB dissolved in 200 mL of deionized water, resulting in an initial TOC of approximately 60 mg L^{-1}, calculated based on the molecular formula of MB (C$_{16}$H$_{18}$ClN$_3$S) and its carbon fraction ($\sim$60%).

Photocatalytic degradation was carried out under visible light irradiation with the NiO/GO/SA nanocomposite as the catalyst. At predetermined time intervals (0, 30, 60, 120, and 210 min), aliquots of 5 mL were withdrawn from the reaction mixture and immediately filtered through a 0.22 μm membrane filter to remove catalyst particles and prevent further photocatalytic reaction.

2.6 Fabrication nanocomposite-modified electrode for enhanced charge transfer kinetics

The working electrode was prepared by dispersing 0.1 g of the synthesized nanocomposite and 0.05 g of carbon black in a mixture of 500 μL Nafion 117 binder and 500 μL ethanol, followed by sonication for 30 min to achieve homogeneity. The slurry was drop-cast onto a glass substrate, dried at 60 °C for 2 hours, and secured with adhesive tape. Electrochemical measurements were performed in a three-electrode system using 1 M NaOH (prepared in 200 mL DI water) as the electrolyte, with the nanocomposite-coated glass as the working electrode, a Pt wire as the counter electrode, and Ag/AgCl as the reference electrode. Electrochemical impedance spectroscopy (EIS) was conducted at open-circuit potential with a 10 mV amplitude across a frequency range of 100 kHz to 0.1 Hz to evaluate charge transfer properties.
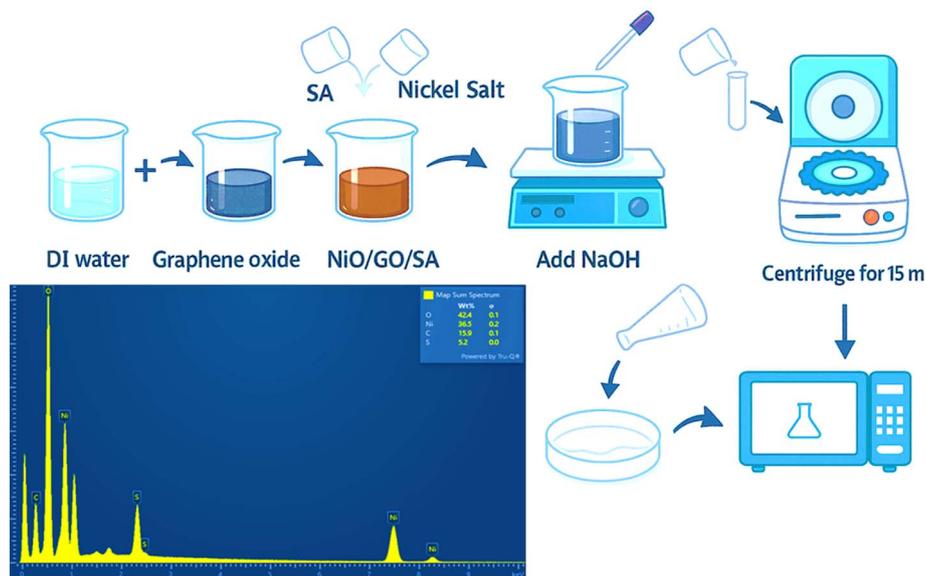
Fig. 1 Graphical representation of the synthesis of the ternary nanocomposite.

3 Results and discussion

3.1 SEM

SEM micrographs of the NiO/GO/SA composite (Fig. 2(a–c)) reveal a heterogeneous morphology, with particles distributed across wrinkled graphene oxide (GO) sheets and interspersed with needle-like sulfanilic acid (SA)-derived structures. The low-magnification image (Fig. 2(a)) highlights the composite's

porous architecture, which is beneficial for catalytic and adsorption applications due to enhanced surface accessibility. Higher-resolution images (Fig. 2(b and c)) provide detailed insights into interfacial interactions and the characteristic wrinkling of defect-rich GO sheets.

The particle size of the composite, measured from SEM images, was found to be 7.6 ± 3.9 μm, with a size distribution ranging from 2.7 to 16.7 μm (Fig. 2(c)). The uniform distribution
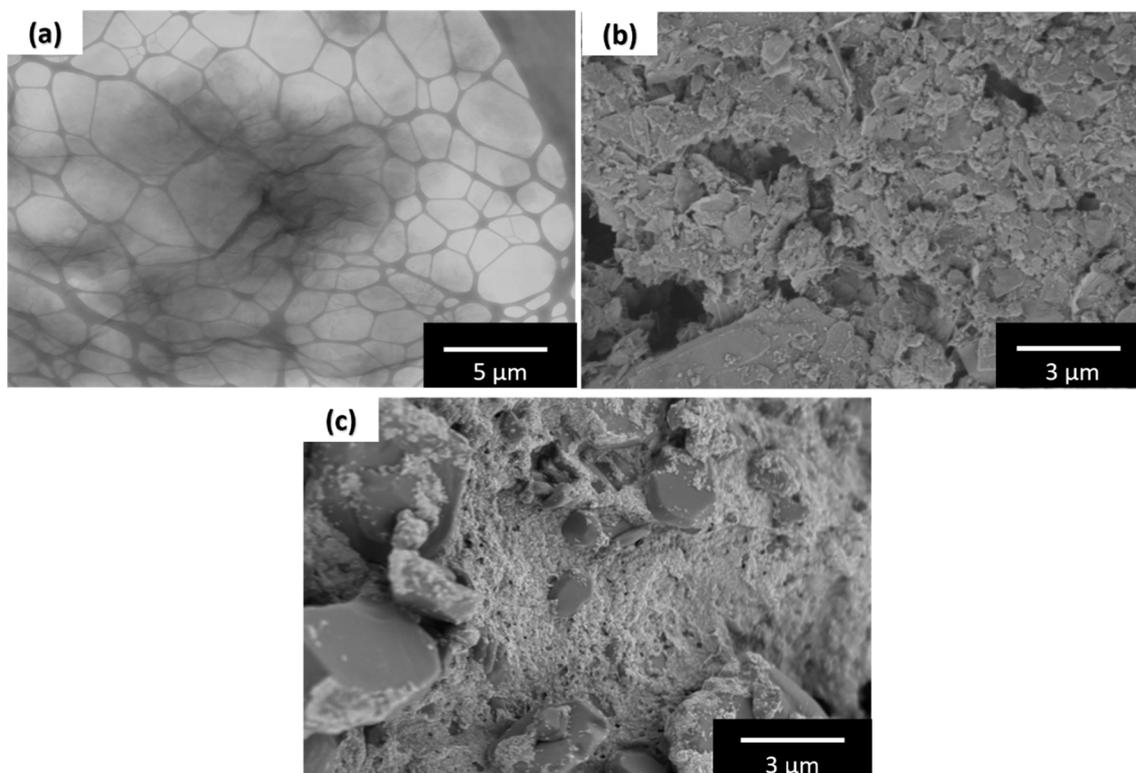

Fig. 2 SEM micrographs of the (a): graphene oxide (b): sulfanilic acid (c): ternary compound (NiO/GO/SA).

of NiO on GO, along with SA-induced morphological features, confirms successful composite formation and suggests synergistic effects that could enhance photocatalytic and adsorption performance.

3.2 XRD

The crystallographic properties for the synthesized materials were examined using X-ray diffraction, with patterns for individual components and the composite shown in Fig. 3(a–c). Pure NiO (Fig. 3(a)) exhibits peaks at $2\theta = 37.2°$ (111), 43.3° (200), 62.9° (220), 75.4° (311), and 79.4° (222), corresponding to the face-centered cubic (FCC) structure of bunsenite (JCPDS No. 01-073-1513). The sharp peaks indicate high crystallinity, with the dominant (200) reflection suggesting preferential growth along this plane. The absence of impurities confirms phase purity. The SA pattern (Fig. 3(b)) shows peaks at $2\theta = 16.8°$ (101), 23.2° (202), and 28.6° (220), characteristic of a monoclinic

system (JCPDS No. 00-031-1897). The strong (002) reflection at 14.3° indicates layered stacking *via* hydrogen bonding and π–π interactions. The composite pattern (Fig. 3(c)) confirms successful integration, with NiO peaks remaining prominent but reduced in intensity due to dilution effects (see Table 1). The broad GO (002) peak at ~10.8° suggests partial oxidation and disordered stacking, while diminished SA peaks indicate molecular-level dispersion. New reflections at 24.5° (010) and 32.7° (202) suggest interfacial interactions.

The crystallite size (D) of NiO in the composite was estimated using the Debye–Scherrer eqn (1):

$$D = \frac{k\lambda}{\beta \cos \theta} \tag{1}$$

where λ is the X-ray wavelength (Cu Kα = 1.5406 Å), β is the full width at half maximum (FWHM) in radians, and θ is the Bragg angle. The calculated average crystallite size for NiO in the ternary composite is ~18–22 nm, slightly smaller than that of
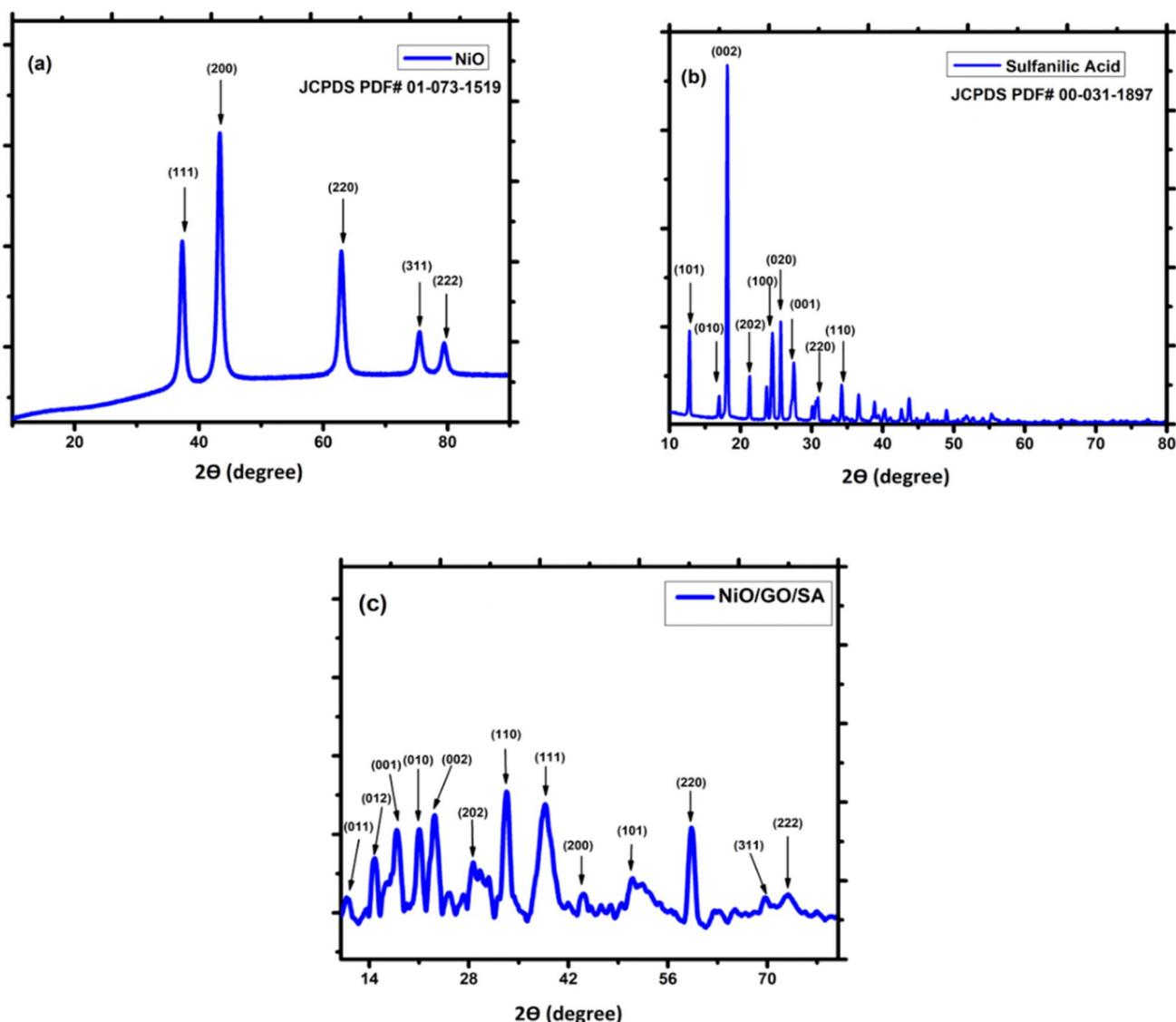

Fig. 3 XRD spectrum of (a) NiO (b) sulfanilic acid (c) ternary compound (NiO/GO/SA).

Table 1 XRD analysis used to determine the *hkl* values of ternary composite

2θ Values (degree)	θ (degree)	(hkl) Values
17	8.5	001
21	10.5	010
28	13.5	202
38	19	111
44	21.5	200
59	30	220
73	36.5	222

pure NiO (∼25 nm), indicating lattice strain and interfacial interactions with GO and SA. Broadening of GO and SA peaks further supports partial disorder and molecular-level dispersion within the composite. These findings quantitatively support the presence of strong interfacial interactions in the ternary system.

Peak broadening implies reduced crystallite size and strain effects from composite formation. A crystallinity of a material is calculated by using this eqn (2):

$$Crystallinity = \frac{Area\ of\ crystalline\ peak}{Area\ of\ all\ crystalline\ peak} \times 100 \quad (2)$$

The crystallinity observed is 83%. The highest peak observed in a ternary composite is at 101 at 38°. The advantage of using co-precipitation method is that it removes all the functional groups, results a successful adornment of graphene oxide on the surface and the suppression peak of graphene oxide in the composition of nanocomposite.[22]

3.3 EDS

SEM-EDX analysis of the NiO/GO/SA ternary composite (Fig. 4) revealed a heterogeneous elemental distribution with oxygen (42.4 wt%), nickel (36.5 wt%), carbon (15.9 wt%), and sulfur (5.2 wt%). Ni signal appear weak in certain EDS regions due to surface roughness or peak overlap, but quantitative XPS analysis confirms the presence of Ni in the composite. The oxygen content reflects contributions from both GO and NiO, while the sulfur content confirms the presence of sulfonic acid groups from SA. Nitrogen was not reliably detected in EDX; however, XPS analysis confirms the presence of amine groups from SA. The O/C ratio (∼2.6) reflects the oxidized structure of GO along with NiO, and the N/S ratio (∼8) highlights the dominant amine functionality of SA. These results collectively confirm the successful formation of the ternary NiO/GO/SA composite.

3.4 Raman spectroscopy

Raman spectroscopy (as shown in Fig. 5(a–c)) was employed to investigate vibrational properties. Pure NiO (Fig. 5(a)) exhibits phonon modes at 550 cm^{-1} (LO), 1105 cm^{-1} (TO + LO), and 1486 cm^{-1} (2LO), confirming its crystalline fcc structure. The broad 550 cm^{-1} peak suggests lattice defects or strain. SA (Fig. 5(b)) shows characteristic peaks at 818 cm^{-1} (ring deformation), 1033–1062 cm^{-1} (SO$_3^-$ stretching), and 3064 cm^{-1} (aromatic C–H stretching), confirming its structural integrity. The composite spectrum (Fig. 5(c)) reveals successful integration: (1) NiO signatures shift to 831 cm^{-1} (interfacial strain) and 1130 cm^{-1} (NiO–GO interaction); (2) GO's D (1343 cm^{-1}) and G (1603 cm^{-1}) bands appear, with an ID/IG ratio of 1.2 (moderate disorder enhances charge transfer between NiO, GO, and SA, supporting improved catalytic and sensing performance); (3)
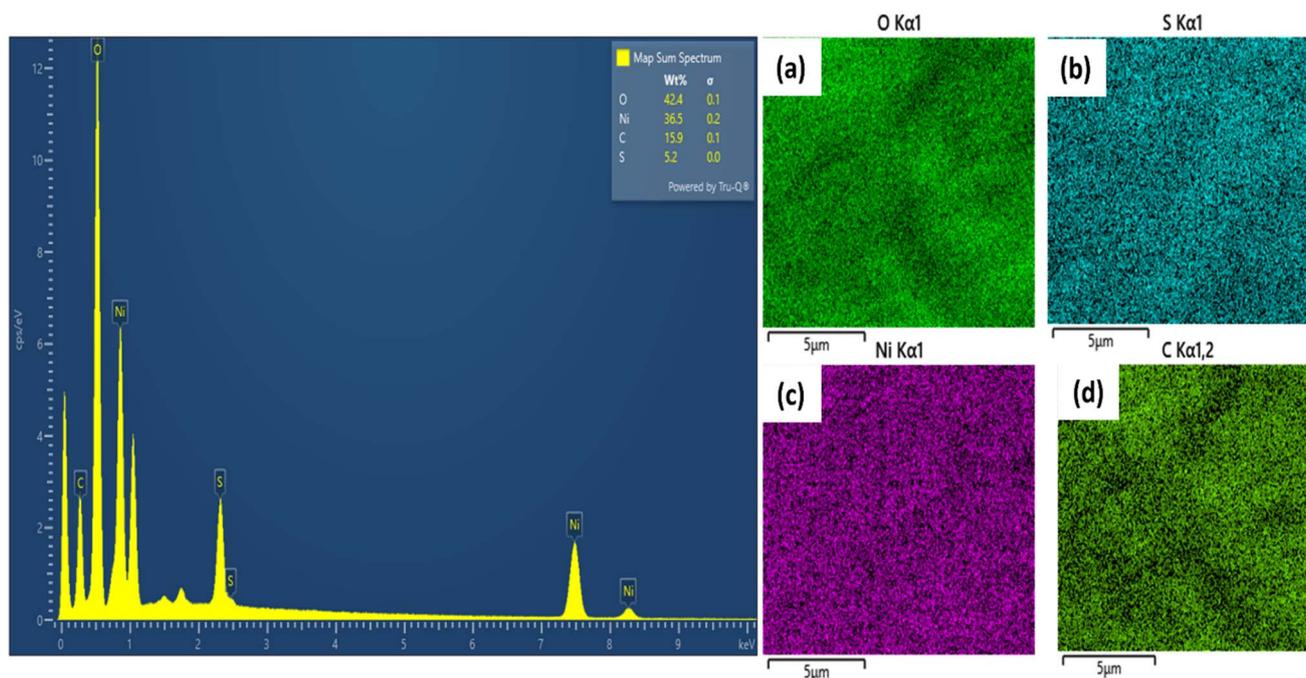

Fig. 4 Elemental composition and microanalysis (a) oxygen (b) sulfer (c) nickel (d) carbon of ternary composite (NiO/GO/SA).
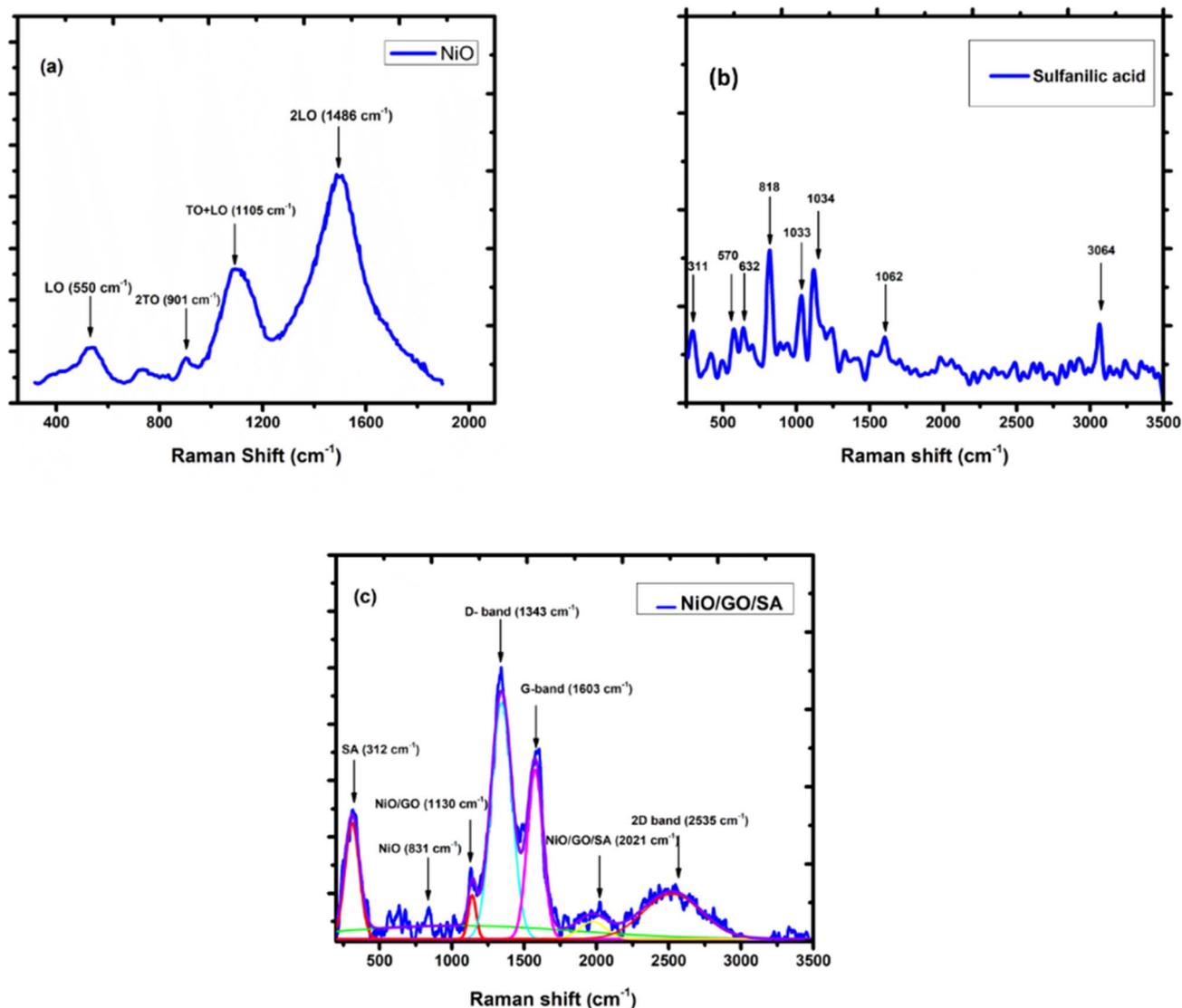
Fig. 5   Raman spectrum of (a) NiO (b) sulfanilic acid (c) ternary compound (NiO/GO/SA).

residual SA vibrations persist at 312 cm^{-1} (SO_3^- bending); and (4) new modes emerge at 2021 cm^{-1} (combination band) and 2535 cm^{-1} (2D overtone), suggesting 3–5 layer GO with moderate oxidation. These findings confirm a strongly interacting ternary system with modified vibrational properties, likely enhancing catalytic/sensing performance.

3.5   FTIR

Pure SA (as shown in Fig. 6(a)) exhibits O–H stretching (3450 cm^{-1}), N–H stretching (3200–3100 cm^{-1}), aromatic C=C (1620 cm^{-1}), S=O (1380 cm^{-1}), and S–O (1150 cm^{-1}) vibrations, confirming sulfonate and amine groups. FTIR spectra (Fig. 6(b)) reveal chemical bonding and functional group interactions in the NiO/GO/SA composite. The NiO/GO spectrum shows O–H (3400 cm^{-1}), C=O (1720 cm^{-1}), C=C (1620 cm^{-1}), C–O (1050 cm^{-1}), and Ni–O (500–900 cm^{-1}) bands. In the composite, SA (1380 cm^{-1}) and GO (1720 cm^{-1}) vibrations persist, while the

Ni–O band shifts to 550 cm^{-1}, indicating interfacial bonding. Additionally, raman spectra of the composite show NiO-related vibrational modes at 694 and 831 cm^{-1}, consistent with reported Ni–O stretching, further confirming the presence of NiO in the ternary system.[23] New peaks at 1250 cm^{-1} (C–N) and 1450 cm^{-1} (COO$^-$) suggest chemical interactions between SA's amine and GO's oxygen groups. The broadened 3400 cm^{-1} band indicates enhanced hydrogen bonding. These results confirm a chemically bonded ternary composite with modified interfacial properties, where covalent linkages and hydrogen bonding between components enhance functional performance in catalysis/adsorption.

3.6   XPS spectroscopy

XPS analysis of the ternary NiO/GO/SA composite (as shown in Fig. 7(a–f)) revealed distinct chemical states and interfacial interactions. Ni 2p spectra (Fig. 7(a)) exhibited characteristic
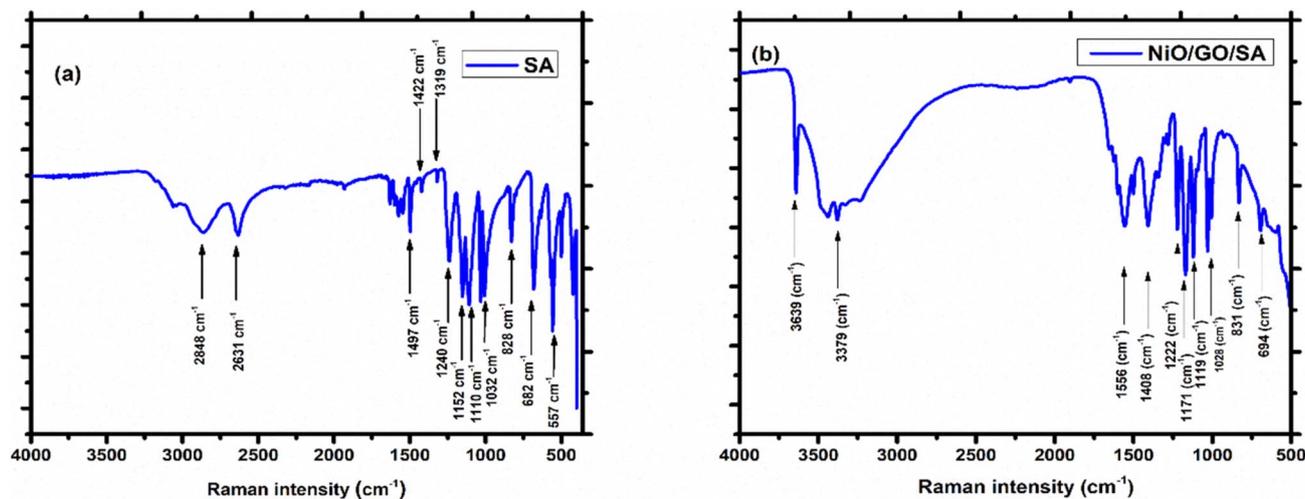
Fig. 6   FTIR spectrum of (a) sulfanilic acid (b) ternary compound (NiO/GO/SA).

peaks at 855.3 eV (Ni^{2+} $2p_{3/2}$) and 873.6 eV (Ni^{2+} $2p_{1/2}$) with satellite features (861.3 eV), confirming the dominant presence of NiO. O 1s (Fig. 7(b)) deconvolution resolved lattice oxygen with hydroxyl groups (531.2 eV), and adsorbed water (532.8 eV), reflecting surface hydration. N 1s (Fig. 7(c)) peaks at 399.5 eV (–NH_2 from sulfanilic acid) and 407 eV (graphitic N) confirmed successful integration of SA and N-doping in GO. C 1s spectra (Fig. 7(d)) featured graphitic carbon (285 eV), and carboxylates (288.5 eV), indicative of GO's oxidized framework. S 2p (Fig. 7(e)) showed sulfate component (168.9 eV) indicated partial oxidation. Ternary-specific (Fig. 7(f)) features different peaks confirming Ni $2p_{3/2}$, Ni $2p_{3/2}$, O1s, C1s with high resolution peaks (Table 2) at different binding energies with some satellite peaks These results collectively demonstrate the synergistic chemical landscape driving the material's functional properties.

Importantly, FTIR analysis provided complementary evidence for the retention of amino groups in the composite. In addition to the SA-related N–H stretching (3200–3100 cm^{-1}), the composite spectrum revealed a distinct C–N vibration at 1250 cm^{-1}, consistent with covalent interaction of amine groups with GO's oxygen functionalities. The persistence of both SA (1380 cm^{-1}) and GO (1720 cm^{-1}) characteristic bands, together with the broadened O–H/N–H stretching band (~3400 cm^{-1}), further confirms the coexistence and stabilization of amine functionalities within the GO framework.

These results collectively demonstrate that both XPS and FTIR corroborate the retention and chemical participation of amino groups in the NiO/GO/SA composite, supporting its tailored interfacial properties.

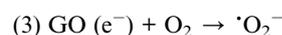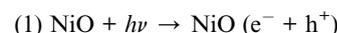### 3.7   UV-vis analysis of photocatalytic degradation of methylene blue

The photocatalytic degradation of methylene blue (MB) using the synthesized NiO/GO/SA nanocomposite (as shown in Fig. 8). Was investigated under visible light irradiation, and the degradation process was monitored using UV-visible spectroscopy. The absorption spectra, as illustrated in Fig. 8(a), reveal

two major characteristic peaks of MB. The first peak, centered around 293 nm, corresponds to π–π* transitions associated with the aromatic rings in the dye structure. The second, and more prominent, peak at approximately 663 nm is attributed to n–π* transitions related to the conjugated structure of methylene blue.

A progressive and systematic decline in absorbance at 663 nm was observed with increasing irradiation time, indicating the breakdown of the conjugated chromophore system of MB. This trend confirms the photocatalytic activity of the NiO/GO/SA nanocomposite, which facilitates the generation of reactive oxygen species (ROS) under light exposure. The observed decline in absorbance at both 293 nm and 663 nm suggests not only the destruction of the chromophoric group but also the breakdown of the aromatic structure, indicating deep degradation rather than simple decolorization.

The near-complete disappearance of the 663 nm peak in the final stages of irradiation suggests substantial degradation of the dye, potentially leading to complete mineralization into non-toxic end products such as CO_2 and H_2O. The enhanced activity of the NiO/GO/SA photocatalyst can be attributed to the synergistic effect among its components. NiO acts as the primary light-absorbing semiconductor, while GO serves as an effective electron acceptor and transport medium, suppressing electron–hole recombination. Meanwhile, sulfanilic acid (SA) enhances hydrophilicity, visible light absorption, and dye adsorption through π–π interactions. Absorption graph with time can be seen in Fig. 8(b).

The proposed mechanism for the photocatalytic degradation of methylene blue by the NiO/GO/SA nanocomposite under visible light is outlined as follows:
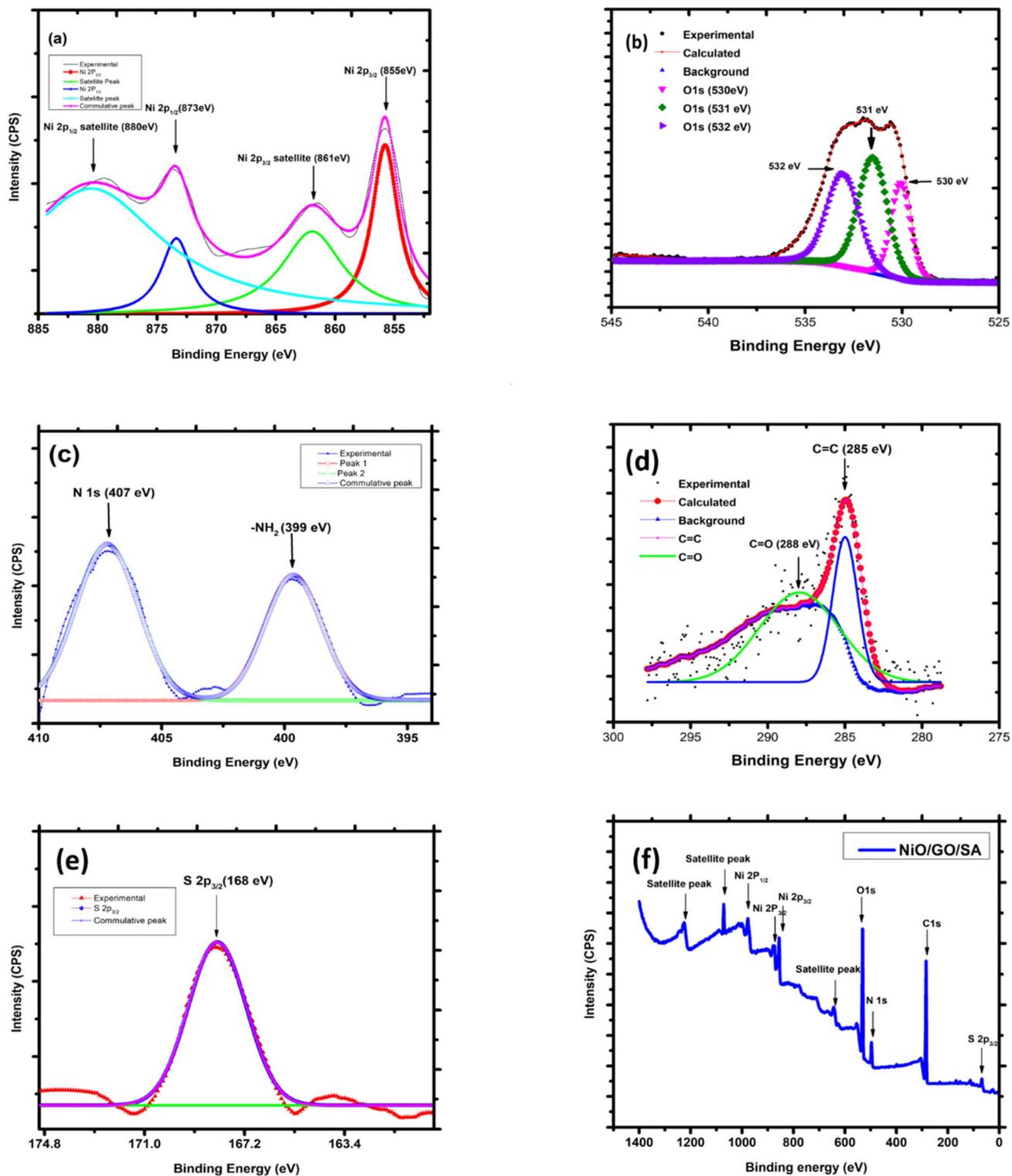
$$(1) \; NiO + h\nu \rightarrow NiO \; (e^- + h^+)$$

$$(2) \; GO + e^- \; (from \; NiO) \rightarrow GO \; (e^-)$$
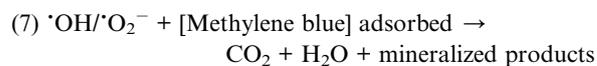
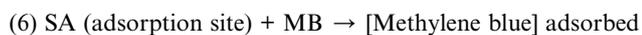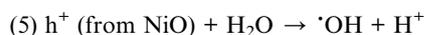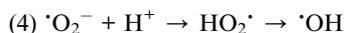$$(3) \; GO \; (e^-) + O_2 \rightarrow {}^{\bullet}O_2{}^-$$

Fig. 7 High resolution XPS spectra for Ni2p (a), O1s (b), N1s (c), C1s (d), S(e), and the survey XPS spectra (f) for the ternary composite (NiO/GO/SA).

$$(4) \; {}^{\bullet}O_2^- + H^+ \rightarrow HO_2^{\bullet} \rightarrow {}^{\bullet}OH$$

$$(5) \; h^+ \text{ (from NiO)} + H_2O \rightarrow {}^{\bullet}OH + H^+$$

$$(6) \; SA \text{ (adsorption site)} + MB \rightarrow \text{[Methylene blue] adsorbed}$$

$$(7) \; {}^{\bullet}OH/{}^{\bullet}O_2^- + \text{[Methylene blue] adsorbed} \rightarrow CO_2 + H_2O + \text{mineralized products}$$

The proposed photocatalytic mechanism involves the excitation of NiO under visible light, generating electron–hole pairs

Table 2 XPS data for High resolution analysis for Ni, O, S, corresponding to ternary composite (NiO/GO/SA)

Name	FWHM eV	Atomic %	Area (P) CPS.eV	Binding energy (eV)
S2p	2.13	0.89	369.77	163.96
C1s	1.43	65.36	14 112.12	281.53
N1s	0.5	0.72	252.56	396.53
O1s	3.07	29.05	16 906.81	527.08
Ni2p	2.59	3.99	14 587.99	849.1

(e^-/h^+). The photogenerated electrons are transferred to graphene oxide (GO), which acts as an electron acceptor, reducing the recombination rate. These electrons react with dissolved oxygen to form superoxide radicals ($^\bullet O_2^-$), which further convert into highly reactive hydroxyl radicals ($^\bullet OH$). Simultaneously, holes in the valence band of NiO oxidize water molecules, producing additional $^\bullet OH$ radicals. Sulfanilic acid (SA) enhances the adsorption of methylene blue (MB) through π–π interactions and hydrogen bonding, bringing dye molecules closer to reactive species. The generated $^\bullet OH$ and $^\bullet O_2^-$ radicals then attack and degrade the adsorbed MB, leading to high mineralization into CO_2 and H_2O. The ternary nanocomposite thus demonstrates a highly effective photocatalytic response, supported by strong absorption reduction and peak disappearance in UV-Vis spectra.

To quantify the degradation efficiency, the absorbance values at 663 nm were analyzed over different irradiation times. The percentage degradation of MB was calculated using eqn (3):[24]

$$\% \text{ degradation} = (A_o - A_t/A_o) \times 100 \quad (3)$$

where A_0: initial absorbance; A_t: absorbance at a given time t. The photodegradation process follows a pseudo-first-order kinetic model,[25] as described by the eqn (4):

$$\ln(C_o/C_t) = kt \quad (4)$$

Radical scavenging experiments (Fig. 9) further confirmed the dominant role of hydroxyl ($^\bullet OH$) and superoxide ($^\bullet O_2^-$) radicals in MB degradation, while photogenerated holes contributed to a lesser extent (IPA → 52%, BQ → 61%, EDTA → 74%) (Fig. 10).

3.8 TOC measurement for mineralization evaluation

TOC measurements were performed to evaluate mineralization and to distinguish true degradation from mere decolorization of methylene blue (MB) (Fig. 11). The experiments were conducted using 0.001 g MB dissolved in 200 mL of deionized water, resulting in an initial TOC calculated as follows. The molecular formula of MB is $C_{16}H_{18}ClN_3S$ (molar mass $\approx$ 319.5 g mol^{-1}), giving a carbon fraction of 192/319.5 $\approx$ 0.60. Therefore, the total carbon present in 0.001 g MB is 0.001 g × 0.60 $\approx$ 0.0006 g = 0.6 mg C. Considering the solution volume of 0.200 L, the initial TOC concentration is approximately 3 mg L^{-1}.

Photocatalytic degradation was carried out under visible light irradiation (80 W m^{-2}) using the NiO/GO/SA nanocomposite as the catalyst. At predetermined time intervals (0, 30, 60, 120, and 210 min), 5 mL aliquots were withdrawn, filtered through a 0.22 μm membrane to remove catalyst particles, and analyzed using a calibrated TOC analyzer. Each measurement was performed in triplicate, and the mean values are reported.

TOC removal increased progressively with irradiation time, indicating substantial mineralization of MB, as summarized below:

Irradiation time (min)	Residual TOC (mg L^{-1})	TOC removal (%)
0	3	0
30	2	28
60	1	52
120	1	71
210	1	82

The percentage of TOC removal was calculated using the following eqn (5):
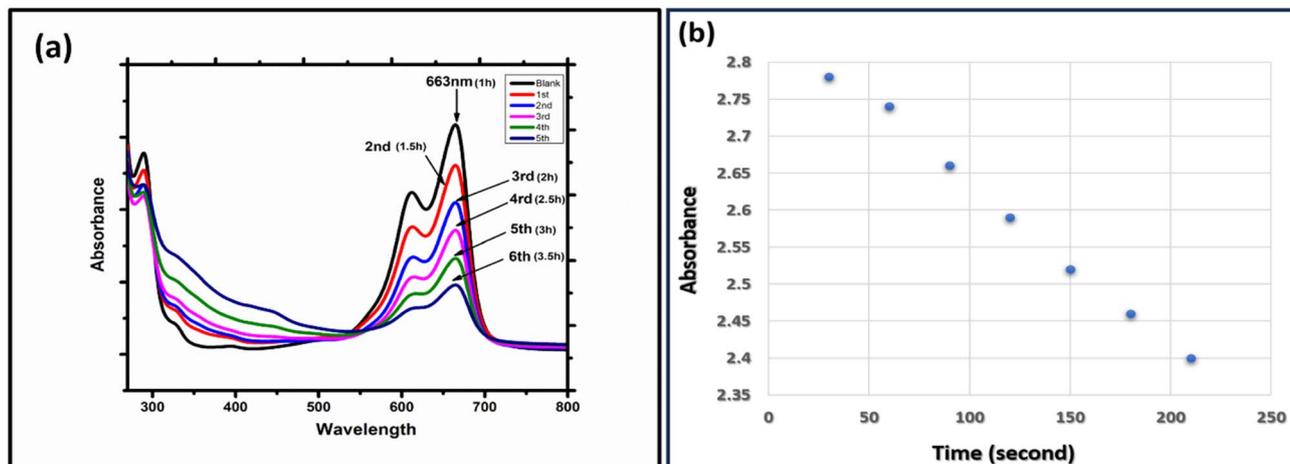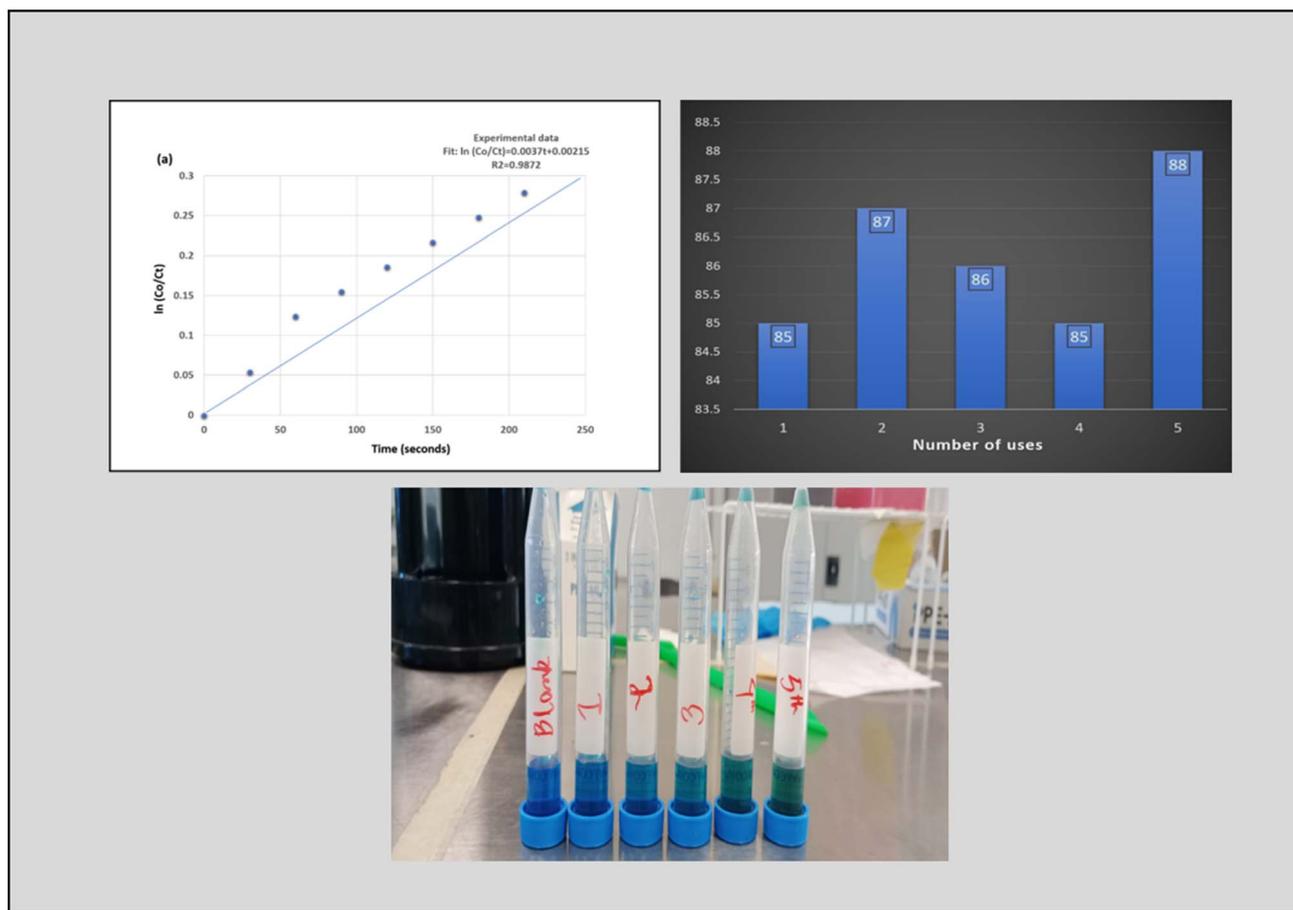

Fig. 8 UV-spectroscopy of (NiO/GO/SA).

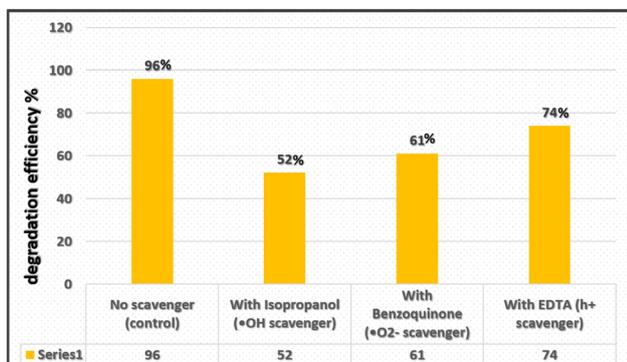Fig. 9 Pseudo first order and reusability of (NiO/GO/SA).

Fig. 10 Photocatalytic degradation of methylene blue over NiO/GO/SA with different scavengers (control, IPA, BQ, EDTA) under visible light.
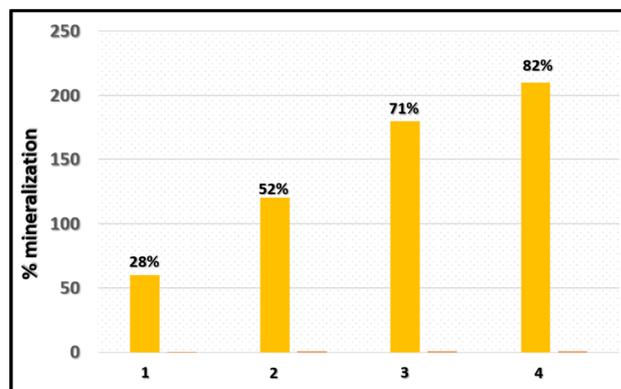

Fig. 11 Percentage mineralization of methylene blue (TOC removal) over NiO/GO/SA under visible-light irradiation at different times.

$$\text{TOC\% removal} = \frac{\text{TOC}_0 - \text{TOC}_t}{\text{TOC}_0} \times 100 \qquad (5)$$

where TOC_0 is the initial TOC concentration (mg L^{-1}) and TOC_t is the TOC concentration at time t (mg L^{-1}). The initial TOC was calculated based on 0.001 g MB dissolved in 200 mL of deionized water. Considering the molecular formula of MB ($C_{16}H_{18}ClN_3S$, molar mass $\approx$ 319.5 g mol^{-1}), the carbon fraction is $\sim$0.60, yielding an initial TOC of approximately 3 mg L^{-1}.

TOC was measured at several irradiation times, with samples filtered to remove the catalyst and analyzed using a calibrated TOC analyzer. TOC removal progressed over time, with residual TOC values of $\sim$2, 1, 1, and 1 mg L^{-1} corresponding to 28%, 52%, 71%, and 82% removal at 30, 60, 120, and 210 min, respectively. These results confirm that the photocatalytic

Table 3 Ternary system studies for efficiency and synthesis method compared with our ternary composite (NiO/GO/SA)

NCs	Synthesis method	Dye	Efficiency	Reference
NiO/Ag/TiO$_2$	Co-precipitation	MB	93%	26
NiO/ZnO/g-C$_3$N$_4$	Hydrothermal	MB	79%	27
(MnO–NiO–ZnO)	Hydrothermal	MB	93%	28
g-C$_3$N$_4$/NiO/ZnO	Co-precipitation	MB	92%	29
NiFe$_2$O$_4$@NiO	Co-precipitation	MB	95%	30
rGO/NiO/Ag	Hydrothermal	MB	95%	31
ZnO : NiO : CuO	Hydrothermal	MB	98%	32
rGO/TiO$_2$/ZnO	Solvothermal	MB	92%	33
NiO/GO/SA	Co-precipitation	MB	96%	**This work**

process leads to extensive mineralization of MB beyond mere decolorization.

The TOC results are fully consistent with the radical scavenger experiments, where photodegradation efficiency decreased in the presence of specific scavengers (control: 96%; IPA → 52%; BQ → 61%; EDTA → 74%). This confirms that $\cdot$OH and $\cdot$O$_2{}^-$ are the primary reactive species responsible for MB degradation.

Different ternary composite with synthesis method is mentioned in Table 3. The NiO/GO/SA nanocomposite achieves 96% methylene blue degradation under visible light outperforming NiO/Ag/TiO$_2$ (93%) and rGO/NiO/Ag (95%). This enhancement originates from synergistic interactions between NiO nanoparticles which generate electron–hole pairs under irradiation, while GO's conductive sp^2 network rapidly transfers electrons, suppressing recombination. Sulfanilic acid simultaneously enhances dye adsorption through π–π stacking (FTIR-confirmed C–N bonding) and improves hydrophilicity. The transferred electrons react with oxygen to yield $\cdot$O$_2{}^-$ radicals, while holes oxidize water to form $\cdot$OH species which is the primary oxidants responsible for MB breakdown, consistent with pseudo-first-order kinetics ($k = 0.032$ min^{-1}) (can be seen in 9b). NiO/GO/SA offers superior visible-light response and retains >85% activity after five cycles (can be seen in 9b) due to GO's stability and SA's protective role, making it a sustainable alternative to toxic-metal photocatalysts. Current limitations in interfacial charge transfer could be optimized through defect engineering.

4 Electrochemical properties of NiO/GO/SA

4.1 Electrochemical impedance spectroscopy (EIS)

Electrochemical impedance spectroscopy (EIS) was conducted under both galvanostatic (GEIS) and potentiostatic (PEIS)
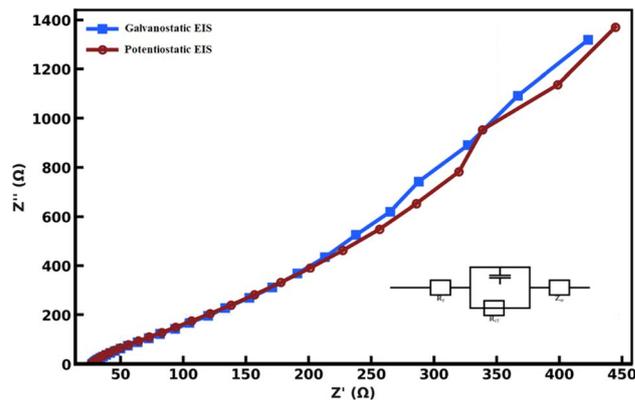

Fig. 12 Galvanostatic EIS and Potentiostatic EIS of ternary compound (NiO/GO/SA).

Table 5 Estimated specific capacitance of the NiO/GO/SA electrode at different scan rates

Scan rate (mV s^{-1})	Estimated C_s (F g^{-1})
5	650
10	575
20	475
30	375
50	275

modes to evaluate the charge-transfer and diffusion processes. The Nyquist plots (Fig. X) were fitted using a Randles-type equivalent circuit consisting of solution resistance (R_s), charge transfer resistance (R_{ct}) in parallel with a double-layer element, and a Warburg diffusion element.

As summarized in Table 4, the solution resistance was nearly identical in both modes ($R_s \approx 27$ Ω), confirming comparable cell/electrolyte contributions. A clear distinction was observed in the charge transfer resistance: GEIS yielded a slightly lower R_{ct} (0.396 kΩ) than PEIS (0.418 kΩ), suggesting marginally faster interfacial kinetics under galvanostatic excitation. The low-frequency intercepts (R_{low-f}) were also consistent with these values (0.423 vs. 0.445 kΩ).

At intermediate to low frequencies, both modes exhibited a diffusion-controlled tail with slopes of 4.18 (GEIS) and 4.08 (PEIS), corresponding to Warburg angles of ~76°. Linear regression of the diffusion regions gave excellent correlation (R^2 > 0.98), confirming well-defined semi-infinite diffusion. Notably, the maximum imaginary impedance reached 1.32 kΩ (GEIS) and 1.37 kΩ (PEIS), in agreement with the fitted

Table 4 Impedance parameters extracted from GEIS and PEIS measurements

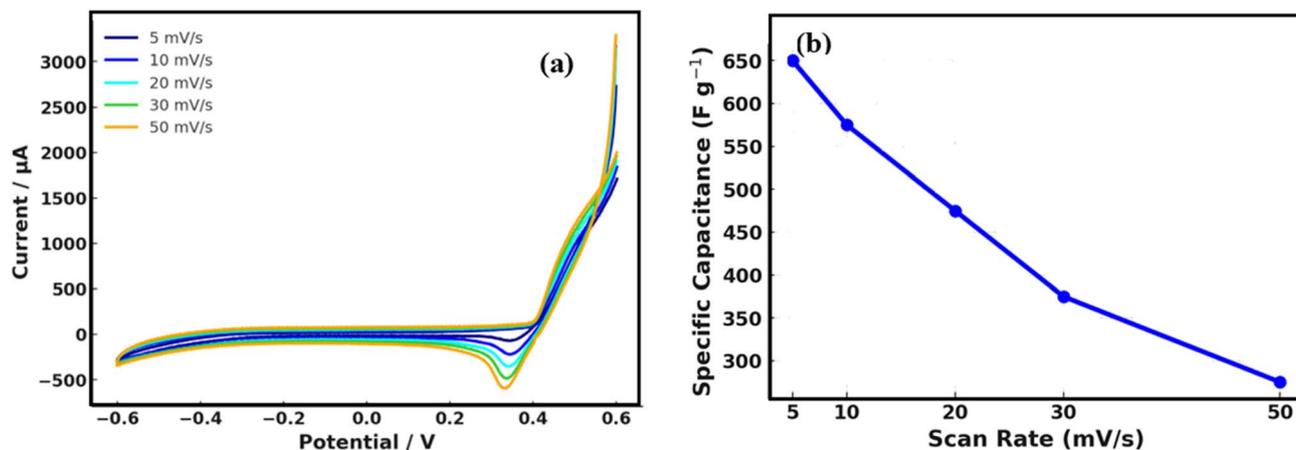| Mode	R_s (Ω)	R_{low-f} (kΩ)	R_{ct} (kΩ)	Z''_{max} (kΩ)	$Z'Z''$ (kΩ)	Warburg slope ($\Delta Z''/\Delta Z'$)	Warburg angle (°)	Warburg line R^2	Z' range (kΩ)	Z'' range (kΩ)
GEIS	27.3	0.423	0.396	1.32	0.422	4.18	76.6	0.99	0.395	1.32
PEIS	26.6	0.445	0.418	1.37	0.444	4.08	76.2	0.98	0.418	1.37

Fig. 13 CV curves (a) and corresponding specific capacitance (b) of the NiO/GO/SA electrode at scan rates of 5–50 mV s^{-1}.

resistances. Overall, both GEIS and PEIS provide consistent impedance features, with GEIS indicating a modest reduction in charge-transfer resistance (Fig. 12).

4.2 Cyclic voltammetry

The cyclic voltammetry of the NiO/GO/SA electrode recorded at scan rates from 5 to 50 mV s^{-1} reveals well-defined anodic and cathodic peaks that are characteristic of the reversible Ni^{2+}/Ni^{3+} redox transition in alkaline media.[34] The anodic peak is centered near 0.4–0.5 V while the cathodic peak appears around 0.2–0.3 V, confirming that the electrode operates through a pseudocapacitive mechanism. The progressive increase in current response with increasing scan rate demonstrates that both capacitive and diffusion-controlled charge storage processes are active in the composite. The presence of sulfanilic acid in the hybrid system plays a critical role by introducing SO$_3$H and –NH$_2$ functional groups onto graphene oxide, which enhances electrolyte wettability, provides additional ion-accessible sites, and promotes uniform dispersion of NiO. As a result, the electrode shows improved ionic diffusion and faster electron transport, which is reflected in the relatively narrow peak-to-peak separation and good reversibility of the redox couple even at higher scan rates.[35]

The electrode delivered a high specific capacitance of ∼650 F g^{-1} at 5 mV s^{-1}, which gradually decreased to ∼575, 475, 375, and 275 F g^{-1} at 10, 20, 30, and 50 mV s^{-1}, respectively. This reduction at higher scan rates is attributed to insufficient time for electrolyte ions to diffuse into the inner pores of the electrode, restricting charge storage to the outer surface. The specific capacitance can be calculated by integrating the area under the CV curve and normalizing by the scan rate, potential window, and mass of the active material according to the equation $C_s = \int I(V) \mathrm{d}V / 2m\nu\Delta V$. In addition, the relationship between peak current and scan rate can be analyzed using the power law $I_p = a\,\nu^b$. A slope value close to 1 when plotting $\log I_p$ against $\log \nu$ indicates surface-controlled capacitive storage, while a slope close to 0.5 corresponds to diffusion-controlled charge transfer. For NiO/GO/SA, the mixed slope values

typically fall between 0.6 and 0.9, suggesting a combination of both mechanisms, with the contribution of GO and sulfanilic acid shifting the balance toward capacitive control. A further level of analysis can be carried out by separating the current response into capacitive and diffusion contributions using the relationship $i(V) = k_1\nu + k_2\,\nu^{1/2}$. This method reveals that at low scan rates, the diffusion-controlled contribution is dominant, while at higher scan rates, the surface-controlled component becomes increasingly significant, which is consistent with the role of GO and –SO$_3$H functional groups in facilitating rapid charge transfer. The peak-to-peak separation, ΔE_p, also provides insight into reaction kinetics, with smaller values at low scan rates indicating fast electron transfer and slight increases at high scan rates reflecting diffusion limitations. If the electrode mass or geometric area is known, these calculations can be extended to report specific capacitance in F g^{-1} or areal capacitance in F cm^{-2}. Thus, the CV analysis of NiO/GO/SA not only confirms the pseudocapacitive behavior of the composite but also quantifies the synergistic role of sulfanilic acid and graphene oxide in enhancing conductivity, ionic accessibility, and overall electrochemical performance. As summarized in Table 5, the NiO/GO/SA electrode delivered a high specific capacitance of 650 F g^{-1} at 5 mV s^{-1}, which gradually decreased to 275 F g^{-1} at 50 mV s^{-1}, consistent with the diffusion limitations typically observed in pseudocapacitive systems. Fig. 13 CV curves (a) and corresponding specific capacitance (b) of the NiO/GO/SA electrode at scan rates of 5–50 mV s^{-1}.

5 Conclusion

This study demonstrates the successful fabrication and multi-functionality of a NiO/GO/SA ternary nanocomposite synthesized *via* co-precipitation. Structural analysis confirmed uniform NiO distribution on GO sheets with sulfanilic acid functionalization, leading to reduced crystallite size (∼18–22 nm), 83% crystallinity, and strong interfacial bonding. Elemental and spectroscopic studies (SEM-EDX, Raman, FTIR, and XPS) validated the integration of Ni, O, C, S, and N functionalities that underpin the synergistic properties of the

composite. The photocatalytic evaluation revealed superior activity toward methylene blue degradation (96% removal, $k = 0.032$ min^{-1}) with 82% TOC mineralization, surpassing several reported ternary nanocomposites. The mechanism involved efficient electron–hole separation by GO, adsorption enhancement *via* sulfanilic acid, and radical-driven degradation. Excellent reusability (>85% activity retention after five cycles) further supports its practical potential. Electrochemical characterization confirmed its pseudocapacitive nature, delivering a high specific capacitance of 650 F g^{-1} at 5 mV s^{-1}, maintaining 275 F g^{-1} at 50 mV s^{-1}, and exhibiting stable ion diffusion and charge transfer with low R_{ct} ($\sim$0.4 kΩ). These combined photocatalytic and electrochemical performances establish NiO/GO/SA as a versatile nanocomposite suitable for wastewater treatment, pollutant mineralization, and energy storage applications. Future work should focus on defect engineering and optimized interfacial design to further enhance charge-transfer efficiency.

Conflicts of interest

There is no conflict of interest.

Data availability

All data is already available in the paper.

Acknowledgements

References

1 H. B. Slama, *et al.*, Diversity of synthetic dyes from textile industries, discharge impacts and treatment methods, *Appl. Sci.*, 2021, **11**(14), 6255, DOI: **10.3390/app11146255**.

2 M. Chowdhury, *et al.*, Characterization of the effluents from leather processing industries, *Environ. Process.*, 2015, **2**(1), 173–187, DOI: **10.1007/s40710-015-0065-7**.

3 W. U. Khan, *et al.*, A critical review of hazardous waste generation from textile industries and associated ecological impacts, *J. Indian Chem. Soc.*, 2023, **100**(1), 100829, DOI: **10.1016/j.jics.2022.100829**.

4 K. Singh and S. Arora, Removal of synthetic textile dyes from wastewaters: a critical review on present treatment technologies, *Crit. Rev. Environ. Sci. Technol.*, 2011, **41**(9), 807–878, DOI: **10.1080/10643380903218376**.

5 A. Negi, Environmental impact of textile materials: challenges in fiber–dye chemistry and implication of microbial biodegradation, *Polymers*, 2025, **17**(7), 871, DOI: **10.3390/polym17070871**.

6 A. Mills, *et al.*, Effect of alkali on methylene blue (CI Basic Blue 9) and other thiazine dyes, *Dyes Pigments*, 2011, **88**(2), 149–155, DOI: **10.1016/j.dyepig.2010.05.015**.

7 I. Khan, *et al.*, Review on methylene blue: its properties, uses, toxicity and photodegradation, *Water*, 2022, **14**(2), 242, DOI: **10.3390/w14020242**.

8 G. Bal and A. Thakur, Distinct approaches of removal of dyes from wastewater: A review, *Mater. Today Proc.*, 2022, **50**, 1575–1579, DOI: **10.1016/j.matpr.2021.09.119**.

9 N. M. Chauke, *et al.*, Harnessing visible light: enhancing TiO2 photocatalysis with photosensitizers for sustainable and efficient environmental solutions, *Front. Chem. Eng.*, 2024, **6**, 1356021, DOI: **10.3389/fceng.2024.1356021**.

10 R. Marschall, Semiconductor composites: strategies for enhancing charge carrier separation to improve photocatalytic activity, *Adv. Funct. Mater.*, 2014, **24**(17), 2421–2440, DOI: **10.1002/adfm.201303214**.

11 J. Ahmad, K. Majid and M. A. Dar, Controlled synthesis of p-type NiO/n-type GO nanocomposite with enhanced photocatalytic activity and study of temperature effect on the photocatalytic activity of the nanocomposite, *Appl. Surf. Sci.*, 2018, **457**, 417–426, DOI: **10.1016/j.apsusc.2018.06.200**.

12 S. M. Meybodi, *et al.*, Synthesis of wide band gap nanocrystalline NiO powder via a sonochemical method, *Ultrason. Sonochem.*, 2012, **19**(4), 841–845, DOI: **10.1016/j.ultsonch.2011.11.017**.

13 F. Mustafa, *et al.*, Synthesis and characterization of wide band gap nickel oxide (NiO) powder via a facile route, *Optik*, 2017, **140**, 38–44, DOI: **10.1016/j.ijleo.2017.04.029**.

14 K.-Q. Lu, *et al.*, Roles of graphene oxide in heterogeneous photocatalysis, *ACS Mater. Au*, 2021, **1**(1), 37–54, DOI: **10.1021/acsmaterialsau.1c00022**.

15 X. Li, *et al.*, Graphene in photocatalysis: a review, *Small*, 2016, **12**(48), 6640–6696, DOI: **10.1002/smll.201600382**.

16 G. Liu, *et al.*, Unique physicochemical properties of two-dimensional light absorbers facilitating photocatalysis, *Chem. Soc. Rev.*, 2018, **47**(16), 6410–6444, DOI: **10.1039/C8CS00396C**.

17 Y. Slimani, *et al.*, Exploration of electronic and vibrational properties of sulfanilic acid through periodic and non-periodic DFT calculations, *J. Mol. Model.*, 2024, **30**(5), 121, DOI: **10.1007/s00894-024-05911-6**.

18 A. Beagan, *et al.*, Amine and sulfonic acid functionalized mesoporous silica as an effective adsorbent for removal of methylene blue from contaminated water, *J. King Saud Univ. Sci.*, 2022, **34**(2), 101762, DOI: **10.1016/j.jksus.2021.101762**.

19 V. B. Cashin, *et al.*, Surface functionalization and manipulation of mesoporous silica adsorbents for improved removal of pollutants: a review, *Environ. Sci.: Water Res. Technol.*, 2018, **4**(2), 110–128, DOI: **10.1039/C7EW00322F**.

20 H. M. Hassan, *et al.*, Sulfanilic acid-functionalized magnetic GO as a robust adsorbent for the efficient adsorption of methylene blue from aqueous solution, *J. Mol. Liq.*, 2022, **361**, 119603, DOI: **10.1016/j.molliq.2022.119603**.

21 E. Huitrón-Segovia, *et al.*, Influence of raw material on the morphology and photocatalytic properties of graphene oxide, *Diam. Relat. Mater.*, 2025, **152**, 111951, DOI: **10.1016/j.diamond.2025.111951**.

22 H. Sadiq, *et al.*, Assessment of antioxidant activity of pure graphene oxide (GO) and composite V2O5/GO using DPPH radical and H2O2 scavenging assays, *J. Sol. Gel Sci. Technol.*, 2023, **108**(3), 840–849, DOI: **10.1007/s10971-023-06231-6**.

23 A. Rahdar, M. Aliahmad and Y. Azizi, NiO Nanoparticles: Synthesis and Characterization, *J. Nanostruct.*, 2015, **5**(2), 145–151, DOI: **10.7508/jns.2015.02.009**.

24 C. P. Y. Kong, *et al.*, Auramine O UV photocatalytic degradation on TiO2 nanoparticles in a heterogeneous aqueous solution, *Catalysts*, 2022, **12**(9), 975.

25 A. H. Jawad, *et al.*, Kinetics of photocatalytic decolourization of cationic dye using porous TiO2 film, *J. Taibah Univ. Sci.*, 2016, **10**(3), 352–362, DOI: **10.1016/j.jtusci.2015.03.007**.

26 W. Mohammed, *et al.*, Visible light photocatalytic degradation of methylene blue dye and pharmaceutical wastes over ternary NiO/Ag/TiO2 heterojunction, *ACS omega*, 2023, **8**(43), 40063–40077, DOI: **10.1021/acsomega.3c01766**.

27 R. Jayaprakash, *et al.*, Hydrothermally constructed and visible-light activated efficient NiO/ZnO/g-C3N4 ternary nanocomposites for methylene blue dye degradation and antibacterial applications, *Inorg. Chem. Commun.*, 2024, **159**, 111643, DOI: **10.1016/j.inoche.2023.111643**.

28 P. Barooah, *et al.*, Waste biomass-based graphene oxide decorated with ternary metal oxide (MnO-NiO-ZnO) composite for adsorption of methylene blue dye, *Clean. Water*, 2024, **2**, 100049, DOI: **10.1016/j.clwat.2024.100049**.

29 N. Bano, R. Fatima, U. Bilal, T. Abbas, A. S. S. Bilal and I. Hussain, Fabrication of G-C3N4/NiO/ZnO Based Ternary Nanocomposite for Efficient Photocatalytic Degradation of Methylene Blue, In Review October, 21, 2024, DOI: **10.21203/rs.3.rs-5250401/v1**.

30 G. Rana, P. Dhiman, A. Kumar, E. A. Dawi and G. Sharma, Structural, optical, electrical properties and photocatalytic performance of Ni-Mg-Zn nano ferrites for tetracycline degradation, *Chemical Physics Impact*, 2024, **8**, 100507, DOI: **10.1016/j.chphi.2024.100507**.

31 D. Singh, *et al.*, Enhancement of the photocatalytic activity of rGO/NiO/Ag nanocomposite for degradation of methylene blue dye, *RSC Adv.*, 2024, **14**(4), 2429–2438, DOI: **10.1039/d3ra07000j**.

32 M. Z. Ishaque, *et al.*, Fabrication of ternary metal oxide (ZnO: NiO: CuO) nanocomposite heterojunctions for enhanced photocatalytic and antibacterial applications, *RSC Adv.*, 2023, **13**(44), 30838–30854, DOI: **10.1039/d3ra05170f**.

33 N. Raghavan, S. Thangavel and G. Venugopal, Enhanced photocatalytic degradation of methylene blue by reduced graphene-oxide/titanium dioxide/zinc oxide ternary nanocomposites, *Mater. Sci. Semicond. Process.*, 2015, **30**, 321–329.

34 Y. Liu, *et al.*, Nickel oxide/graphene composites: synthesis and applications, *Chem.–Eur. J.*, 2019, **25**(9), 2141–2160.

35 X. Hui, *et al.*, Fast fabrication of NiO@ graphene composites for supercapacitor electrodes: Combination of reduction and deposition, *Mater. Des.*, 2016, **109**, 242–250.